

Oxygen vacancy formation and annihilation in lanthanum cerium oxide as a metal reactive oxide on 4H-silicon carbide

Cite this: *Phys. Chem. Chem. Phys.*, 2014, 16, 7015

Way Foong Lim and Kuan Yew Cheong*

Received 11th December 2013,
Accepted 27th January 2014

DOI: 10.1039/c3cp55214d

www.rsc.org/pccp

A mechanism regarding the redox reaction in lanthanum cerium oxide ($\text{La}_x\text{Ce}_y\text{O}_z$) post-deposition annealed in reducing and oxidizing atmosphere was schematized and discussed in association with the presence of lanthanum as a substitutional cation. Analyses have been performed using X-ray diffraction, energy-filtered transmission electron microscopy, scanning transmission electron microscope-energy dispersive spectroscopy line scan, and capacitance–voltage measurements. The results showed the presence of an oxygen vacancy when La^{3+} was in its substitution site, while annihilation of oxygen vacancy was accompanied by a displacement of La^{3+} from the substitutional site to the interstitial site via a kick-out mechanism prior to its disappearance from the CeO_2 .

1 Introduction

Keeping pace with the prevalent application of cerium oxide (CeO_2), straddling areas from catalysis^{1,2} to solid oxide fuel cells,³ gas sensors,⁴ and more recently as a passivation^{5,6} and catalytic layer,^{7,8} or the so-called metal reactive oxide on semiconductor substrates, the inherent properties of CeO_2 associated with its reversible change from the +4 to +3 oxidation state have been unveiled. Oxygen vacancies have been found as the indispensable key defects in CeO_2 , coupling with changes between the two oxidation states (Ce^{4+} to Ce^{3+}) in order to achieve the desired redox-ability in the oxide.^{9–11} Hitherto, numerous research investigations have conclusively deduced the improvement in oxygen vacancies after the addition of aliovalent cations to the oxide.^{12–14}

Kaspar *et al.*¹ indicated that doping of CeO_2 with foreign cations would offer different benefits from the catalytic features of CeO_2 , which include oxygen storage capacity, surface reducibility, and oxygen mobility.^{15–20} On the other hand, if an isovalent cation is introduced to the CeO_2 lattice, limited oxygen vacancy concentration will be induced²¹ due to the absence of a charge compensation mechanism. For instance, the doping of Zr^{4+} into the CeO_2 lattice has proved that doped CeO_2 is better than pure CeO_2 in terms of the lowering of the Ce^{4+} reduction energy or oxygen vacancy formation energy, which would enhance the kinetics of Ce^{4+} reduction, but additional oxygen vacancies are not created. Therefore, it is preferable to dope CeO_2 with lower

valence cations that can eventually increase the oxygen vacancy concentration in the CeO_2 . The consideration has been shrunk down to trivalent cations since bivalent dopants like Ca^{2+} that have been doped into CeO_2 are thermally unstable, and thus phase segregation happened and the oxygen migration became more difficult.^{21–23}

Various trivalent cations can be doped into CeO_2 , which include Sm^{3+} , Y^{3+} , La^{3+} , Lu^{3+} , Yb^{3+} , Er^{3+} , and Gd^{3+} . Particular consideration is focused on the La^{3+} cation in this work is due to its widespread use in the high dielectric constant (k) mixed oxides in metal-oxide-semiconductor (MOS) based devices, which include $\text{La}_2\text{Zr}_2\text{O}_7$,^{24–26} LaAlO_3 ,^{27–29} and $\text{La}_2\text{Hf}_2\text{O}_7$.^{30–32} The investigation of La^{3+} -doped CeO_2 as the high k gate oxide material in MOS based devices have not been explored by other researchers. Furthermore, the improved catalytic property of CeO_2 after doping with La^{3+} has heightened further investigation on La^{3+} -doped CeO_2 as a high k metal reactive oxide on a 4H-SiC substrate for the development of a 4H-SiC-based MOS capacitor gas sensor.

Several studies regarding the incorporation of trivalent lanthanum cations (La^{3+}) into CeO_2 to form lanthanum cerium oxide ($\text{La}_x\text{Ce}_y\text{O}_z$) solid solutions have been carried out.^{14,32–35} Previous literatures have included atomistic simulations and theories to investigate the materials aspect of the La^{3+} -doped CeO_2 . It is noteworthy from first principles density functional theory reported by Nakayama and Martin³⁶ that defect association and migration energy is strongly dependent on ionic radius of the cation, wherein a smaller size causes trapping of the oxygen vacancy at the next nearest site of the dopant while a larger size decreases the trapping effect but causes an increase in the migration energy. Nevertheless, the extent to

Electronic Materials Research Group, School of Materials & Mineral Resources Engineering, Universiti Sains Malaysia, Engineering Campus, 14300 Nibong Tebal, Penang, Malaysia. E-mail: cheong@eng.usm.my, wayfoong317@yahoo.com.sg; Fax: +604-5941011; Tel: +604-5995259

which the redox-ability of the resulting oxide goes is dependent on the dominance of the effect. Redox-ability can be improved when there are a large amount of oxygen anions which are mobile and are distributed randomly through the CeO_2 lattice through migration. Doping of the CeO_2 lattice in this work with La^{3+} which is larger in ionic radius (0.118 nm) when compared with Ce^{4+} (0.097 nm) may decrease the defect association energy but in the mean time increase the migration energy, which may reduce the oxygen mobility in the lattice. Nonetheless, there exists a trade-off relationship whereby the distribution of La^{3+} in CeO_2 lattice needs to be taken into consideration. It was shown by Heinmaa *et al.*³⁵ via ^{17}O high resolution magic angle spinning nuclear magnetic resonance analysis that La^{3+} distribution in the lattice is almost random. Oxygen migration can happen either in the CeO_2 lattice between the regular oxygen sites or between occupied and vacant oxygen sites, depending on the doping level of La^{3+} . It was deduced that the calculated migration energy is within 0.45 and 0.96 eV. These values are in agreement with the findings from Nakayama and Martin.³⁶ Structural evidences have been used to deduce that the distribution of La^{3+} in the CeO_2 lattice is random³⁵ and in particular the formation of oxygen vacancies^{14,32,37} is accompanied by a reduction of the Ce^{4+} to Ce^{3+} states.¹⁴ Whilst this phenomenon may be the primary defect mechanism in $\text{La}_x\text{Ce}_y\text{O}_z$, other related studies have been performed, and utilization of the oxide for carbon monoxide adsorption³² has been used to successfully detect the location of oxygen vacancies in the oxide. Following findings from Heinmaa *et al.*³⁵ regarding oxygen anion migration via a hopping mechanism, O'Neill and Morris¹⁴ further supported the idea that the oxygen anions are mobile and are distributed randomly through the CeO_2 lattice. On the other hand, phenomena associated with oxidation from the Ce^{3+} to Ce^{4+} states have been reported by utilizing $\text{La}_x\text{Ce}_y\text{O}_z$ for soot oxidation³⁸ in ambient oxygen. This reversed transformation from Ce^{3+} to Ce^{4+} states happens as a result of an oxygen exchange between the ambient gas phase oxygen and lattice oxygen in the oxide. A similar oxidation was carried out by Fleming *et al.* with the exception that the oxide was subjected to oxygen exposure after argon treatment.³⁹ The oxidation process has been described as a surface-mediated process, however there is no evidence to justify the idea that there are remaining oxygen vacancies after the completion of oxidation process.

Although $\text{La}_x\text{Ce}_y\text{O}_z$ has been studied both theoretically and experimentally, the contribution of La^{3+} in the CeO_2 lattice, which may involve more complex defect chemistry than has been expected, is scant. Therefore, the present work is focused on further exploration of this aspect. In this work, a detailed mechanism involving redox that elaborates the function of lanthanum in perturbing the CeO_2 lattice and facilitating the removal of oxygen as well as the dwindling of lanthanum and oxygen vacancies from the CeO_2 lattice after oxygen gain is presented. The suggested mechanism is based on theoretical findings from previous literatures and supporting data from the present work. Dissimilar from previous work, which systematically studied $\text{La}_x\text{Ce}_y\text{O}_z$ using atomic simulations

and/or theoretical aspects, the experimental studies of $\text{La}_x\text{Ce}_y\text{O}_z$ deposited on a 4H-SiC substrate in this work have been performed by varying one of the processing parameters, which is by undergoing post-deposition annealing of the sample firstly in a reducing ambient to elaborate the reduction process in the oxide and then in an oxidizing ambient to describe the oxidation process in the oxide.

2 Experimental procedures

In this work, the $\text{La}_x\text{Ce}_y\text{O}_z$ precursor was prepared using a wet chemical route, which is the metal-organic decomposition (MOD) method. Two types of precursors were prepared, one is associated with the cerium-containing precursor and the other one is associated with the lanthanum-containing precursor. The starting reagents used were $[\text{Ce}(\text{acac})_3]$ and lanthanum nitrate hydrate powders. Mixed solvent systems (acetic acid and methanol) were used to ensure the desired dissolution and reaction behaviour. Acetic acid (CH_3COOH) was added to the precursor mixture for suppression of hydrolysis, which in turn results in a precursor species, which is desirable for film formation. Methanol (CH_3OH) was added to control the solution stability. An optimum molarity of 0.25 M of the cerium-containing precursor was prepared by dissolving 1.0936 g of the $\text{Ce}(\text{acac})_3$ powder in 6 ml of CH_3COOH and the mixture was stirred at room temperature for 5 min before CH_3OH (4 ml) was added. The resulting mixture was then heated on a hot plate at 60 °C for 15 min. Simultaneously, different molarities of lanthanum-containing precursor were prepared by mixing an appropriate amount of the lanthanum nitrate hydrate $[\text{La}(\text{NO}_3)_3 \cdot 6\text{H}_2\text{O}]$ powder with an appropriate volume of acetylacetone solution to obtain an acac type of precursor. The solution was stirred at room temperature (r.t.) for 5 min prior to heating on a hot plate for 15 min with continuous stirring. Both precursors were subsequently mixed together in a beaker and stirred continuously at r.t. for another 15 min. After that, the mixture was poured into a round bottom flask, which was placed on a heating mantle. The mixture was lastly subjected to a reflux process at 130 °C for 2 h to allow the chelating process between two precursors to occur and so to obtain a more attractive final solution in terms of solution stability and film formation behaviour. The resulting $\text{La}_x\text{Ce}_y\text{O}_z$ precursor was cooled down prior to spin-coating on a RCA (Radio Corporation of America)-cleaned, 4.09°-off (0001) oriented, n-type Si-faced 4H-SiC substrate at a spinning rate and time of 4000 rpm and 30 s, respectively. After spinning, the samples were post-deposition annealed (PDA) at 1000 °C in ambient forming gas (FG; 95% N_2 -5% H_2) and ambient oxygen [99.999% oxygen (O_2)] (heating and cooling rate = 5 °C min⁻¹) for 15 min.

An X-ray diffraction system (P8 Advan-Bruker) was used to characterize the presence of phase and orientation of $\text{La}_x\text{Ce}_y\text{O}_z$ film (scan range of $2\theta = 25$ –60°; step time = 71.60 ms; step size $2\theta = 0.0322^\circ$). Cross-sectional studies of the $\text{La}_x\text{Ce}_y\text{O}_z$ /4H-SiC were performed using energy filtered (Zeiss Libra 200)

transmission electron microscopy (EFTEM) operated at 200 kV. Initially, a protective layer of resist and platinum was sputtered on the top surface of the $\text{La}_x\text{Ce}_y\text{O}_z$ films deposited on the 4H-SiC substrates. Subsequently, the samples were placed in a chamber for an ion milling process using a focused ion beam (FIB). The FIB was used to prepare TEM lamella samples using approximately 30 kV and 65 nA for voltage and current of the ion beam, respectively. The lamella sample, once finished thinning, was transferred to a TEM copper (Cu) grid using platinum deposition. Final thinning was performed on the lamella sample using an ion beam at 5 kV and current 81 pA. Subsequently, the Cu grid holding the TEM lamella samples was inserted into the TEM chamber. The oxide and IL thickness of the investigated samples were measured using ImageJ software. Scanning TEM mode (STEM; FEI Tecnai TF-20) with a high-angle annular dark field (HAADF) detector was used to obtain full 0–20 keV energy dispersive X-ray spectroscopy (EDS) spectra for line scan analysis on the samples. Impedance-capacitance-resistant (ICR) meter (Agilent 4284) and a semiconductor parameter analyzer (Keithley 4200-SCS) were utilized to measure the high frequency (1 MHz) C - V measurements on $\text{Al}/\text{La}_x\text{Ce}_y\text{O}_z/4\text{H-SiC}$ metal-oxide-semiconductor (MOS) capacitors by sweeping the gate voltage bi-directionally from -4 to 4 V. Flatband voltage shift (ΔV_{FB}) of the C - V curves can be used to calculate effective oxide charges (Q_{eff}) present in the oxide, which includes the oxide fixed charge, oxide trapped charge, and any mobile ionic charge⁴⁰ using eqn (1)

$$Q_{\text{eff}} = \Delta V_{\text{FB}} C_{\text{ox}} / q A_{\text{G}} \quad (1)$$

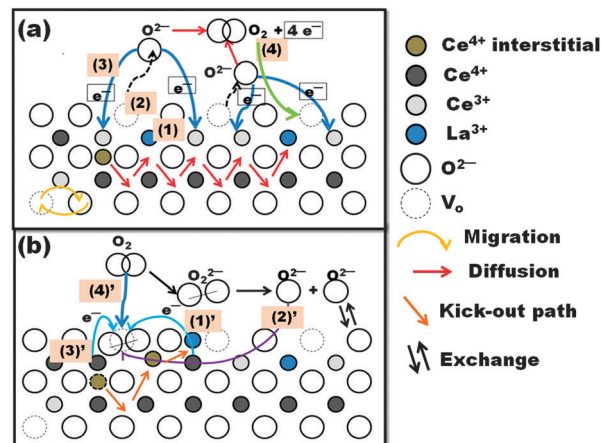
where C_{ox} is the oxide capacitance, q is the electronic charge, and A_{G} is the area of capacitor.

3 Results and discussion

In order to obtain deep insights into the redox reaction in $\text{La}_x\text{Ce}_y\text{O}_z$, the effects of post-deposition annealing in ambient FG and O_2 have been investigated. A plausible mechanism consisting of four elementary steps to elaborate the reaction is schematized in Scheme 1(a) and (b).

Scheme 1(a) is referred to as the reduction process in $\text{La}_x\text{Ce}_y\text{O}_z$ that has been PDA in ambient FG. The mechanism initiates with (1) substitution of Ce^{4+} cations with trivalent La^{3+} cations, (2) formation of oxygen vacancies, (3) transition from Ce^{4+} to Ce^{3+} states, and/or (4) re-oxidation.

Due to a similarity in ionic radius between La^{3+} (0.118 nm) and Ce^{4+} (0.097 nm) cations, a substitutional solid solution is formed, whereby the La^{3+} would substitute Ce^{4+} in the CeO_2 lattice (Step 1). It has been reported that $\text{La}_x\text{Ce}_y\text{O}_z$ is a solid solution⁴¹ of La_2O_3 in CeO_2 and thus the crystal structure of $\text{La}_x\text{Ce}_y\text{O}_z$ follows the cubic fluorite structure of CeO_2 [The International Centre for Diffraction Data (ICDD) file no. 00-034-0394]. The formation of $\text{La}_x\text{Ce}_y\text{O}_z$ has been confirmed *via* the detection of X-ray diffraction (XRD) peaks of $\text{La}_x\text{Ce}_y\text{O}_z$, oriented at (111), (200), (220), and (311) planes (Fig. 1(b)).



Scheme 1 (a) Reduction process in $\text{La}_x\text{Ce}_y\text{O}_z$, described from Step (1) to Step (4) and (b) oxidation process in $\text{La}_x\text{Ce}_y\text{O}_z$, described from Step (4') to Step (1') following the opposite sequence in (a).

The substitution of Ce^{4+} into the CeO_2 lattice by La^{3+} would lead to a localized distortion and therefore enlarging octahedral site of unit cell in the cubic fluorite lattice of CeO_2 .³⁷ With these, it is not surprising to have a larger lattice parameter in $\text{La}_x\text{Ce}_y\text{O}_z$. Supporting evidence can be obtained through the XRD peaks' shifts of $\text{La}_x\text{Ce}_y\text{O}_z$ (Fig. 1(b)) to lower diffraction angles with respect to those of CeO_2 .¹¹ In addition, the interplanar spacing, d , of crystalline regions observed in bulk oxide using a cross-sectional EFTEM image (Fig. 2(a) and (b)) has been measured and compared with the calculated d values of $\text{La}_x\text{Ce}_y\text{O}_z$ using Bragg's law. The measured d values (0.28–0.36 nm) are comparable with the calculated d values of $\text{La}_x\text{Ce}_y\text{O}_z$ oriented in (111) (0.33 nm) and (200) (0.28 nm) planes. Additional XRD peaks associated with lanthanum silicate ($\text{La}_{9.33}\text{Si}_6\text{O}_{26}$) with an ICDD no. 00-049-0443 oriented in the (022) plane and 4H-SiC (0001) with an ICDD no. 00-022-1317 are also detected. The formation of $\text{La}_{9.33}\text{Si}_6\text{O}_{26}$ has been discussed elsewhere.^{42,43}

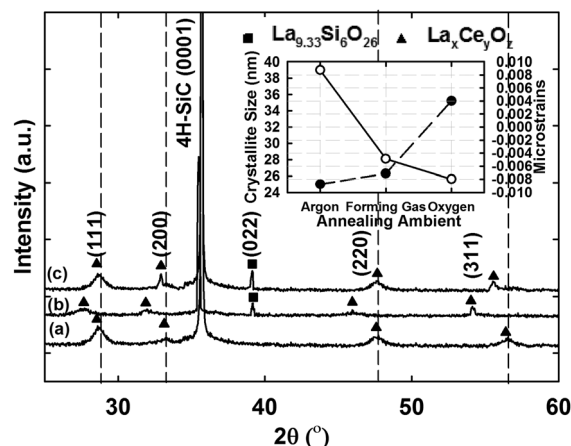


Fig. 1 X-ray diffraction patterns of $\text{La}_x\text{Ce}_y\text{O}_z$ PDA in ambient (a) Ar, (b) FG, and (c) O_2 . The inset shows the calculated crystallite size and microstrains of $\text{La}_x\text{Ce}_y\text{O}_z$ using a Williamson–Hall approach.

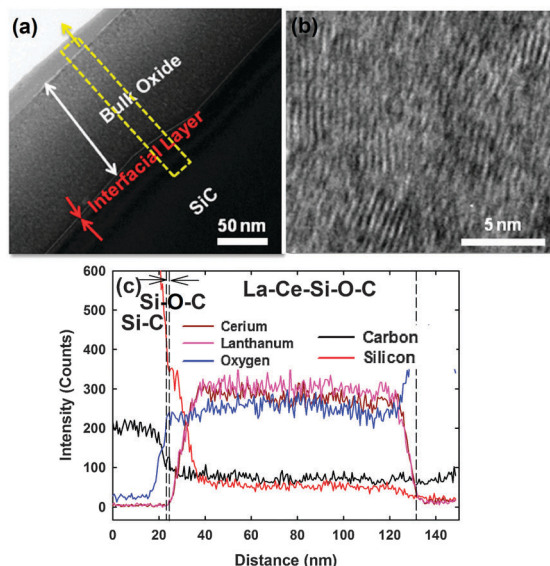


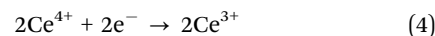
Fig. 2 Cross-sectional EFTM (a) image and (b) zoomed in image and (c) EDS line scan of $\text{La}_x\text{Ce}_y\text{O}_z$ PDA in ambient FG. The yellow rectangle and arrow indicate respectively the area of interest and direction for the line scan.

According to Kroger–Vink notation,⁴⁴ substitution of Ce^{4+} in CeO_2 by La^{3+} cation would lead to the formation of oxygen vacancies and the release of O_2 gas molecules (eqn (2)).



where $\text{Ce}_{\text{Ce}}^{\times}$ is neutral Ce on the Ce lattice; $V_{\text{O}}^{\bullet\bullet}$ is the oxygen vacancy on the oxygen site with a charge of +2, Ce_{Ce}' and La_{Ce}' denote Ce on the Ce site and La on the Ce site, respectively. One school of thought indicates that the presence of La^{3+} in the CeO_2 lattice would give rise to $(\text{La}^{3+}-\text{O}^{\text{vacancy}})$ defect centres with the oxygen holes (O^-) compensating for the lower valence La^{3+} .³² Oxygen vacancies may form and lead to $(\text{Ce}^{4+}-\text{O}^{\text{vacancy}})$ defect centres, provided that the associated Ce^{4+} cations are reducible to Ce^{3+} states.³² Studies of $\text{La}_x\text{Ce}_y\text{O}_z$ as a function of post-deposition annealing temperature in argon (Ar) ambient has deduced the co-existence of Ce^{4+} and Ce^{3+} states with predominant Ce^{3+} states in the oxide based on an X-ray photoelectron spectroscopy (XPS) depth profiling analysis of Ce 3d core level spectra.⁴³ Moreover, the acquisition of a negative flatband voltage shift of capacitance–voltage (C – V) curves supports the existence of positively charged defect centres in the oxide.⁴⁵ These clues have pre-determined that the oxygen vacancies are dominant in the oxide when compared with oxygen holes. Oxygen vacancies are doubly positively charged since two electrons carried by oxygen anion (O^{2-}) that should occupy the site are missing. The formation of the oxygen vacancy (Step 2) is due to the removal of one oxygen anion (O^{2-}) from the CeO_2 lattice when La^{3+} substitutes Ce^{4+} in the lattice. The two electrons are then transferred to neighbouring Ce^{4+} cations, followed by reduction of the Ce^{4+} states to Ce^{3+} states (Step 3). The occurrence of this is attributed to the localization of two electrons from the p orbital of the oxygen anion to 4f orbitals of

Ce^{4+} , leading to the formation of Ce^{3+} , according to the localization concept proposed by Skorodumova *et al.*⁴⁶ The disappearance of electrons from the anion forms the O_2 , according to eqn (3) and (4).



It was proposed that the O_2 gas molecules can either diffuse outward to the oxide surface or diffuse inward to the oxide–4H–SiC interface. The outward diffusing O_2 gas molecules can be re-captured by the oxide at the surface through adsorption at the surface oxygen vacancies (Step 4). Adsorption of O_2 molecules at the oxygen vacancies may form active oxygen species, which are the O_2^- and/or O_2^{2-} ions, according to density functional theory calculations performed by Chen *et al.*⁴⁷ These active oxygen species may subsequently dissociate to O^{2-} and be incorporated into the oxide, depending on the available oxygen vacancy sites for the adsorption of O_2 gas.

In this work, in order to prove that oxygen vacancies are formed in the $\text{La}_x\text{Ce}_y\text{O}_z$ PDA in ambient FG, effective oxide charges (Q_{eff}) present in the oxide are calculated based on the flatband voltage shift of the C – V curve in Fig. 3. It is worth noting that positive Q_{eff} have been perceived, further assuring us of the presence of oxygen vacancies in $\text{La}_x\text{Ce}_y\text{O}_z$. Nevertheless, the C – V curve of $\text{La}_x\text{Ce}_y\text{O}_z$ PDA in ambient Ar is shifted to the more negative side,⁴⁵ indicating the presence of a higher amount of oxygen vacancies in the oxide. Supporting evidence can be obtained by approximating the concentration of oxygen vacancies based on principle component analysis, outlined by Holgado *et al.*⁴⁸ using the equation $[V_{\text{O}}] = 19.6 \times 1.6^{-D}$ where $[V_{\text{O}}]$ is the oxygen vacancy concentration and D is the crystallite size. The Williamson–Hall approach has been adapted to calculate the D from line broadening of the XRD peaks.⁴⁹ The results indicate that the D of $\text{La}_x\text{Ce}_y\text{O}_z$ PDA in FG (26.3 nm) is greater than that in ambient Ar (25.0 nm, inset of Fig. 1). The calculated $[V_{\text{O}}]$ is therefore 4.26 for FG and 4.59 for Ar.

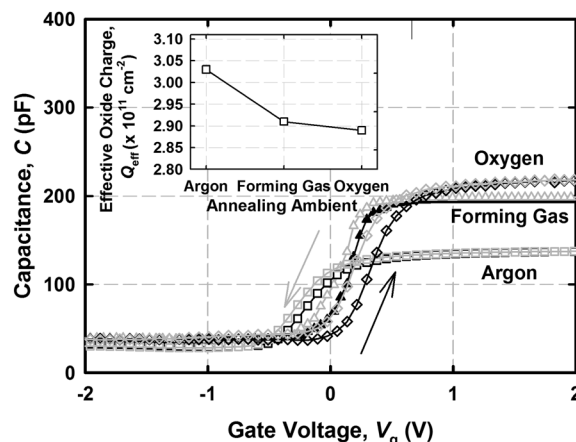
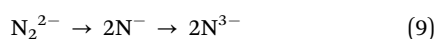
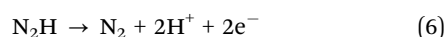
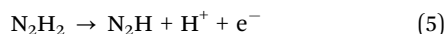


Fig. 3 High frequency (1 MHz) capacitance–gate voltage (C – V) curves of $\text{La}_x\text{Ce}_y\text{O}_z$ PDA in ambient Ar,⁴⁵ FG, and O_2 . The inset shows the calculated effective oxide charge from the flatband voltage shift of the C – V curves.

Apart from these, the decrease in total oxide thickness (120.6 nm) measured from the cross-sectional EFTEM image for FG-annealed $\text{La}_x\text{Ce}_y\text{O}_z$ (Fig. 2(a)) when compared with the cross-sectional high resolution TEM (HRTEM) image of Ar-annealed $\text{La}_x\text{Ce}_y\text{O}_z$ (138.0 nm)⁴³ has suggested an improvement in the oxide density, which can be related to a reduction in $[V_{\text{O}}]$.

In addition, formation of a thin interfacial layer (IL) at the $\text{La}_x\text{Ce}_y\text{O}_z/4\text{H-SiC}$ interface, shown by cross-sectional EFTEM image in Fig. 2(a) for the sample post-deposition annealed in ambient FG was detected. This IL was determined by EDS line scan analysis (Fig. 2(c)) as the Si–O–C IL. The emergence of the Si–O–C IL is believed to be due the oxidation effect brought either by the inward diffusing O_2 gas molecules and active oxygen species (from the oxide) or oxygen molecules from the ambient gas. The latter assumption is eliminated, attributed to the absence of oxidizing species from the post-deposition annealing ambient, which is the ambient FG. Therefore, it is mentioned that the inward diffusing O_2 gas molecules and active oxygen species are responsible for the growth of the Si–O–C IL.

Apparently, post-deposition annealing of the $\text{La}_x\text{Ce}_y\text{O}_z$ in ambient FG should have created a higher amount of oxygen vacancies than that in ambient Ar since FG is an oxygen poor condition. The attainment of an opposite finding suggests the occurrence of the following mechanism that relates with of the FG molecules on oxygen vacancies in $\text{La}_x\text{Ce}_y\text{O}_z$. During post-deposition annealing of the $\text{La}_x\text{Ce}_y\text{O}_z$ deposited on the 4H-SiC in ambient forming gas, which is comprised of N_2 and H_2 , two plausible phenomena may happen, in which the N_2 – H_2 gas molecules may or may not interact with the inward and/or outward diffusing O_2 gas molecules, followed by adsorption on oxygen vacancy site. The interaction of N_2 – H_2 molecules with O_2 may happen, due to a higher electronegativity value of O (3.44) when compared with N (3.04) and H (2.20). These $\text{N}_2\text{H}_2\text{O}_2$ gas molecules are subsequently adsorbed on the oxygen vacancies of $\text{La}_x\text{Ce}_y\text{O}_z$. In the former case, the resulting adsorbed products may be N_2 and H_2O while in latter case, N_2 and H_2 are formed. These assumptions are made based on the dehydrogenation process, which may happen, as conveniently described by Huang *et al.*,⁵⁰ whereby N_2 and H^+ are formed (eqn (5)). The process is a proton transfer process, in which the H^+ may bind to O_2 gas molecules (eqn (6)) and form H_2O , which becomes vapour gas and disappears from the lattice, leaving N_2 and electrons in the lattice (eqn (7)). The evaporation of H_2O may happen since the post-deposition annealing temperature (1000 °C) used is much higher than the boiling temperature of H_2O . The N_2 may combine with the electrons and form N_2^{2-} (eqn (8)). Subsequent incorporation of the N_2^{2-} into the bulk oxide forms N^{3-} (eqn (9)). The reduction of N_2^{2-} to 2N^{3-} may happen when two neighbouring Ce^{4+} cations transfer two electrons to 2N^{2-} .



The N^{3-} ions may substitute into the oxygen vacancies in the lattice. The N^{3-} is plausible to substitute into the oxygen vacancies since N^{3-} with an ionic radius of 143 pm can accommodate the vacancies previously occupied by O^{2-} anions with an ionic radius of 140 pm. It is foreseen that substitution of N^{3-} in one oxygen vacancy will induce the formation of more oxygen vacancies in neighbouring anion sites and the reduced Ce^{3+} cations are oxidized to Ce^{4+} states for charge neutrality. This is an extraordinary condition with the presence of $(\text{Ce}^{4+}-\text{O}^{\text{vacancy}})$ defect centres. Nevertheless, the findings from the Q_{eff} (Fig. 3) calculated from the flatband voltage shift of the $C-V$ curve, which showed a lesser positive charge, allow us to deduce that this assumption may not possible. Moreover, the attainment of a smaller $[V_{\text{O}}]$ in this sample suggested that the N^{3-} anions do not replenish the oxygen vacancies. This is because substitution of the N^{3-} ions would increase the amount of oxygen vacancies in the lattice. Therefore, it is expected that larger positive charges are attained. The acquisition of a lesser positive charges suggested that the nitrogen ions did not take part in oxygen vacancy association. The detection of a thinner Si–O–C IL (1.6 nm) measured from the cross-sectional EFTEM image when compared with the oxide post-deposition annealed in Ar ambient (2.5 nm), which was carried out previously, suggested that the N^{3-} ions reside at the oxide–4H-SiC interface and suppress the growth of the Si–O–C IL by accumulating at the oxide–4H-SiC interface as a barrier layer. The formation of a thinner Si–O–C IL thickness (1.6 nm) in FG-annealed $\text{La}_x\text{Ce}_y\text{O}_z$ measured from the EFTEM image (Fig. 2(a)) than in Ar-annealed $\text{La}_x\text{Ce}_y\text{O}_z$ (2.5 nm)⁴⁴ has supported the hypothesis about N^{3-} anions. The presence of N^{3-} anions at the interface creates repulsive forces to the inward diffusing O_2 and/or adsorbed oxygen species. Therefore, the amount of inward diffusing O_2 and/or adsorbed oxygen species to oxidize 4H-SiC substrate surface^{42,43} for the formation of the Si–O–C IL is decreased. Energy dispersive spectroscopy (EDS) line scan analysis (Fig. 2(c)) acquired from scanning TEM images that are focused by a high-angle annular dark field detector has also shown the detection of the Si–O–C IL.

On the other hand, the oxidation process (Scheme 1(b)) in $\text{La}_x\text{Ce}_y\text{O}_z$ can be described as an opposite process of the four aforementioned steps in Scheme 1, following the sequence from step (4)' to step (1)'. In short, Scheme 1(b) is a recovery process of Scheme 1(a), which brings the entire system close to the original condition of CeO_2 , whereby the La^{3+} cations that have been introduced into the CeO_2 lattice are de-activated. By undergoing post-deposition annealing of $\text{La}_x\text{Ce}_y\text{O}_z$ in ambient O_2 , adsorption of O_2 molecules (Step 4') from the ambient would happen on oxygen vacancies in $\text{La}_x\text{Ce}_y\text{O}_z$. A charge transfer involving electrons from the neighbouring reduced Ce^{3+} cations to the O_2 molecules happens in order to have the O_2 molecules slightly negatively charged (2O_2^-). In this stage, the reduced Ce^{3+} is oxidized back to the Ce^{4+} state (Step 3').

The adsorption process is followed by dissociation to monatomic ions 2O^- that reduces to 2O^{2-} . It is envisioned that either the adsorbed 2O^{2-} ions will fill two oxygen vacancies

or with an oxygen vacancy filled and leaving another O^{2-} diffusing to the bulk oxide or departing as O_2 gas to the surface (Step 2'). At present, justification for the dominance of either of these mechanism remains unclear. Nonetheless, an assumption has been drawn by comparing EDS line scan analysis between $La_xCe_yO_z$ PDA in ambient FG and O_2 (Fig. 2(c) and 4(c)). Based on the EDS line scan analysis, the intensity of O for O_2 -annealed $La_xCe_yO_z$ is lower than FG-annealed $La_xCe_yO_z$. Supposedly, post-deposition annealing in O_2 ambient will supply more O_2 molecules to the oxide. The O_2 molecules once adsorbed either fill one oxygen vacancy or two oxygen vacancies, the resulting positive Q_{eff} in the oxide will become smaller than the FG-annealed $La_xCe_yO_z$. This is in agreement with the calculated Q_{eff} in (Fig. 3) for O_2 -annealed $La_xCe_yO_z$. However, the attainment of a lower intensity of O in EDS line scans for O_2 -annealed $La_xCe_yO_z$ when compared with the FG-annealed $La_xCe_yO_z$ reflects that much of the adsorbed O^{2-} not filling the oxygen vacancies has been missing from the bulk oxide (Fig. 4c). A detailed illustration of the disappearance of O will be discussed in subsequent step (step 1').

Following the re-oxidation of Ce^{3+} to the Ce^{4+} state after the adsorption filling of oxygen vacancies by adsorbed O^{2-} , a charge compensation can be accomplished by forming $[La^{3+}-O^-]$ defect centres, which are similar to the initial condition described when La^{3+} cations are substituting Ce^{4+} in the CeO_2 lattice. Due to the acquisition of the lowest Q_{eff} and lowest $[V_o]$ (2.53) that is calculated by considering D (35.2 nm) from the Williamson–Hall approach, it is undeniable that $[La^{3+}-O^-]$ defect centres may be present in $La_xCe_yO_z$ PDA in ambient O_2 . Conversely, the La profile in the EDS line scan for this sample is relatively low (Fig. 4(c)) when compared with the

$La_xCe_yO_z$ PDA in ambient FG (Fig. 2(c)). This condition is unlikely due to the preparation method of $La_xCe_yO_z$ because the same molar ratio of La:Ce (1:1) has been used for the $La_xCe_yO_z$ PDA in ambient Ar,^{42,43} FG, and O_2 . Due to the utilization of same molar ratio, XPS wide scans of La and Ce have showed comparable intensity of La and Ce in the oxide for Ar-annealed $La_xCe_yO_z$ while the EDS line scan for FG-annealed $La_xCe_yO_z$ (Fig. 2(c)) shows a similar intensity of La and Ce in the bulk oxide. Therefore, it is concluded that some of the substitutional La^{3+} has been withdrawn from the CeO_2 lattice. If this happens, the defect centres will be reduced. In Scheme 1(a), the substitution of Ce^{4+} with La^{3+} has been discussed. This substitution has in fact displaced the Ce^{4+} from the bulk to interstitial sites. When oxidation happens in $La_xCe_yO_z$, for charge neutrality, besides annihilation of oxygen vacancies *via* adsorption filling, a kick-out mechanism^{51,52} will occur. A kick-out mechanism commonly happens when the diffusing interstitial atoms have comparable size with the substitutional impurity atom.^{52,53} In this case, the Ce^{4+} interstitials that are fairly mobile will diffuse around the CeO_2 lattice. When the Ce^{4+} interstitials reach the substitutional La^{3+} , the interstitials will push the substitutional La^{3+} to adjacent interstitial sites (Step 1'). The reduction in intensity of La observed in the EDS line scan (Fig. 4(c)) is explainable when some of the La^{3+} interstitials are diffusing outward to the surface along with C–O that is diffusing outward from the $La_xCe_yO_z/4H-SiC$ interface, as is described in ref. 42 and 43. This can be used to explain the relatively lower intensity of O in $La_xCe_yO_z$ PDA in ambient O_2 . The idea of outward diffusion of the La^{3+} interstitials has been seen in the literatures that have reported about diffusion of titanium interstitials from the bulk oxide to the surface and react with oxygen when the reduced titanium oxide (TiO_2) crystal is annealed in an oxidizing ambient gas.⁵² Unlike the case of TiO_2 , metastable La_2O_3 phases are not detected at the surface of the $La_xCe_yO_z$. Nonetheless, the vanishing of La^{3+} from $La_xCe_yO_z$ is supported *via* the XRD peak shift of $La_xCe_yO_z$ (Fig. 1(b)) to higher diffraction angles, which are closer to the XRD patterns of CeO_2 (Fig. 1(a)). Besides, d values (0.18–0.28 nm) measured from the EFTEM image Fig. 4(a) are matched with the calculated d values for $La_xCe_yO_z$ oriented in (200) (0.27 nm), (220) (0.19 nm), (311) (0.17 nm) planes and $La_{9.33}Si_6O_{26}$ (0.23 nm). Apart from these, cross-sectional EFTEM studies have deduced a decrease in total oxide thickness (94.3 nm) in $La_xCe_yO_z$ PDA in ambient O_2 when compared with $La_xCe_yO_z$ PDA in ambient FG (120.6 nm). This is an indication of an improvement in the oxide density as a result of a decrease in positive Q_{eff} (oxygen vacancies) in $La_xCe_yO_z$ PDA in ambient O_2 (Fig. 2). Above and beyond comparing $La_xCe_yO_z$ PDA in ambient Ar, FG, and O_2 , the calculated microstrain is decreasing with the decrease in Q_{eff} (Fig. 2) but with the increase in D (inset of Fig. 1) from $La_xCe_yO_z$ PDA in ambient Ar to O_2 . This phenomenon is attributed to the ease for agglomeration of neighbouring crystallites when lower amounts of oxygen vacancies are present, as in the O_2 -annealed $La_xCe_yO_z$. The microstrain is reduced in the sample due to a reduction in available oxygen vacancies for migration of O^{2-} to happen.

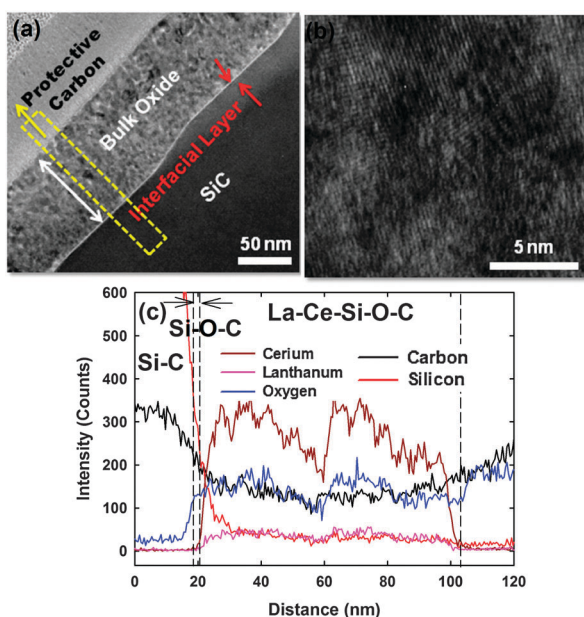


Fig. 4 Cross-sectional EFTEM (a) image and (b) zoomed in image and (c) EDS line scan of $La_xCe_yO_z$ PDA in ambient O_2 . The yellow rectangle and arrow indicate respectively the area of interest and direction for the line scan.

4 Conclusions

In conclusion, the findings from present work have envisaged the occurrence of redox in $\text{La}_x\text{Ce}_y\text{O}_z$, which can be manipulated by changing the processing conditions of $\text{La}_x\text{Ce}_y\text{O}_z$ to being in either a reducing or oxidizing ambient. The redox reaction is a cyclic process, whereby the switching between Ce^{4+} to Ce^{3+} states as well as the kick-out mechanism involving the substitutional and interstitial cations, can be reversed back provided that the La^{3+} cations are still active in the lattice. At present, there is no clear understanding for the de-activation of La^{3+} cations, in which the La^{3+} cations are pushed away from the lattice. Although the proposed model has more spaces for improvement, it provides a framework for better understanding the chemistry of O_2 on $\text{La}_x\text{Ce}_y\text{O}_z$.

Acknowledgements

One of the authors (W. F. Lim) would like to acknowledge financial support given by the Vice Chancellor's Award, USM-RU-PRGS (8043001), and Malaysia Toray Science Foundation (MTSF) grant (6050205).

References

- 1 J. Kaspar, P. Fornasiero and M. Graziani, *Catal. Today*, 1999, **50**, 285–298.
- 2 A. Trovarelli, C. de Leitenburg, M. Boaro and G. Dolcetti, *Catal. Today*, 1999, **50**, 353–367.
- 3 L. Adijanto, A. Sampath, A. S. Yu, M. Cargnello, P. Fornasiero, R. J. Gorte and J. M. Vohs, *ACS Catal.*, 2013, **3**, 1801–1809.
- 4 P. Jasinski, T. Suzuki and H. U. Anderson, *Sens. Actuators, B*, 2003, **95**, 73–77.
- 5 H. J. Quah, K. Y. Cheong, Z. Hassan and Z. Lockman, *J. Mater. Sci.: Mater. Electron.*, 2011, **22**, 583–591.
- 6 W. F. Lim, K. Y. Cheong and Z. Lockman, *Appl. Phys. A: Mater. Sci. Process.*, 2011, **103**, 1067–1075.
- 7 M. Issa, H. Mahzoul, A. Brillard and J.-F. Brilhac, *Chem. Eng. Technol.*, 2009, **32**, 1859–1865.
- 8 S. Jacobsen, U. Helmersson, L. Ekedahl, I. Lundstrom, P. Martensson and A. L. Spetz, *Proceedings of Transducers, The 11th International Conference on Solid-state Transducers*, 2001, pp. 832–835.
- 9 N. V. Skorodumova, S. I. Simak, B. I. Lundqvist, I. A. Abrikosov and B. Johansson, *Phys. Rev. Lett.*, 2002, **89**, 1666011–1666014.
- 10 R. K. Hailstone, A. G. DiFrancesco, J. G. Leong, T. D. Allston and K. J. Reed, *J. Phys. Chem. C*, 2009, **113**, 15155–15159.
- 11 W. F. Lim and K. Y. Cheong, *J. Mater. Sci.: Mater. Electron.*, 2012, **23**, 257–266.
- 12 G. S. Li, Y. C. Mao, L. P. Li, S. H. Feng, M. Q. Wang and X. Yap, *Chem. Mater.*, 1999, **11**, 1259–1266.
- 13 G. R. Rao and B. G. Mishra, *Bull. Catal. Soc. India*, 2003, **2**, 122–134.
- 14 W. M. O'Neill and M. A. Morris, *Chem. Phys. Lett.*, 1999, **305**, 389–394.
- 15 A. Trovarelli, *Comments Inorg. Chem.*, 1999, **20**, 263–284.
- 16 E. Mamontov, T. Egami, R. Brezny, M. Koranne and S. J. Tyagi, *J. Phys. Chem. B*, 2000, **104**, 11110–11116.
- 17 F. Zhang, C.-H. Chen, J. C. Hanson, R. D. Robinson, L. P. Herman and S.-W. Chan, *J. Am. Ceram. Soc.*, 2006, **89**, 1028–1036.
- 18 G. Balducci, J. Kaspar, P. Rofnasiero and M. Graziani, *J. Phys. Chem. B*, 2008, **102**, 557–561.
- 19 W. D. Cai, F. Chen, X. X. Shen, L. J. Chen and J. L. Zhang, *Appl. Catal., B*, 2010, **101**, 160–168.
- 20 M. Biswas and S. Bandyopadhyay, *Mater. Res. Bull.*, 2012, **47**, 544–550.
- 21 M. F. García, A. M. Arias, J. C. Hanson and J. A. Rodriguez, *Chem. Rev.*, 2004, **104**, 4063–4104.
- 22 J. S. Albero, F. R. Reinoso and A. S. Escibano, *J. Catal.*, 2002, **210**, 127–136.
- 23 X.-Q. Wang, J. C. Hanson, G. Liu, J. A. Rodriguez, A. I. Juez and M. F. Garcia, *J. Chem. Phys.*, 2004, **121**, 5434–5444.
- 24 J. M. Gaskell, A. C. Jones, H. C. Aspinall, S. Taylor, P. Taechakumput, P. R. Chalker, P. N. Heys and R. Odedra, *Appl. Phys. Lett.*, 2007, **91**, 112912.
- 25 C. Z. Zhao, S. Taylor, M. Werner, P. R. Chalker, R. T. Murray, J. M. Gaskell and A. C. Jones, *J. Appl. Phys.*, 2009, **105**, 044102.
- 26 J. M. Gaskell, A. C. Jones, P. R. Chalker, M. Werner, H. C. Aspinall, S. Taylor, P. Taechakumput and P. N. Heys, *Chem. Vap. Deposition*, 2007, **13**, 684–690.
- 27 L. Yan, L. B. Kong and C. K. Ong, *Semicond. Sci. Technol.*, 2004, **19**, 935–938.
- 28 K. Kukli, M. Ritala, V. Pore, M. Leskela, T. Sajavaara, R. I. Hegde, D. C. Gilmer, P. J. Tobin, A. C. Jones and H. C. Aspinall, *Chem. Vap. Deposition*, 2006, **12**, 158–164.
- 29 Y.-P. Liu, W. Lan, Z.-W. He and Y.-Y. Wang, *Chin. Phys. Lett.*, 2006, **23**, 2236–2238.
- 30 Y. F. Loo, S. Taylor, R. T. Murray, A. C. Jones and P. R. Chalker, *J. Appl. Phys.*, 2006, **99**, 103704.
- 31 C. Y. Kang, P. D. Kirsch, B. H. Lee, H.-H. Tseng and R. Jammy, *IEEE Trans. Device Mater. Reliab.*, 2009, **9**, 171–179.
- 32 I. Yeriskin and M. Nolan, *J. Chem. Phys.*, 2009, **131**, 2447021–2447026.
- 33 M. Biswas and S. Bandyopadhyay, *Mater. Res. Bull.*, 2012, **47**, 544–550.
- 34 M. R. Benjaram, K. Lakshmi and R. Gode, *Chem. Mater.*, 2010, **22**, 467–475.
- 35 I. Heinmaa, T. Joon, H. Kooskora, J. Pahapill and J. Subbi, *Solid State Ionics*, 2010, **181**, 1309–1315.
- 36 M. Nakayama and M. Martin, *Phys. Chem. Chem. Phys.*, 2009, **11**, 3241–3249.
- 37 L. Liu, X. Way, M. Guo and M. Zhang, *J. Nanosci. Nanotechnol.*, 2011, **11**, 2155–2162.
- 38 A. B. Lopez, K. Krishna, B. van der Linden, G. Mul, J. A. Moulijn and M. Makkee, *Catal. Today*, 2007, **121**, 237–245.
- 39 P. Fleming, S. Ramirez, J. D. Holmes and M. A. Morris, *Chem. Phys. Lett.*, 2011, **509**, 51–57.

- 40 E. H. Nicollian and J. R. Brews, *MOS (Metal Oxide Semiconductor) Physics and Technology*, Wiley, New York, 1982.
- 41 L. Truffault, M.-T. Ta, T. Devers, K. Konstantinov, V. Harel, C. Simmonard, C. Andreazza, I. P. Nevirkovets, A. Pineau, O. Veron and J.-P. Blondeau, *Mater. Res. Bull.*, 2010, **45**, 527–535.
- 42 W. F. Lim and K. Y. Cheong, *J. Phys. Chem. C*, 2013, **117**, 14014–14024.
- 43 W. F. Lim and K. Y. Cheong, *Mater. Chem. Phys.*, 2013, **140**, 622–633.
- 44 X.-Y. Du, W.-C. Li, Z.-X. Liu and K. Xie, *Chin. Phys. Lett.*, 1999, **16**, 376–377.
- 45 W. F. Lim and K. Y. Cheong, *Mater. Res. Soc. Symp. Proc.*, 2012, **1433**, DOI: 10.1557/opl.2012.1114.
- 46 N. V. Skorodumova, S. I. Simak, B. I. Lundqvist, I. A. Abrikosov and B. Johansson, *Phys. Rev. Lett.*, 2002, **89**, 166601.
- 47 H.-T. Chen, J. G. Chang, H. L. Chen and S. P. Ju, *J. Comput. Chem.*, 2009, **30**, 2433–2442.
- 48 J. Holgado, R. Alvarez and G. Munuera, *Appl. Surf. Sci.*, 2000, **161**, 301–315.
- 49 J. Pelleg, E. Elish and D. Mogilyanski, *Metall. Mater. Trans. A*, 2005, **36**, 3187–3194.
- 50 S. X. Huang, T. S. Rufael and J. L. Gland, *Surf. Sci.*, 1993, **290**, L673–L676.
- 51 K. L. Smith and N. Mousseau, *Eur. Phys. J. B*, 2008, **64**, 165–172.
- 52 M. A. Carpenter, S. Mathur and A. Kolmakov, *Metal Oxide Nanomaterials for Chemical Sensors*, Springer, New York, 2013, p. 60.
- 53 M. Nastasi and J. W. Mayer, *Ion Implantation and Synthesis of Materials*, Springer, Berlin, 2006, p. 122.